

Chiral Surface Lattice Resonances

Eric S. A. Goerlitzer, Reza Mohammadi, Sergey Nechayev, Kirsten Volk, Marcel Rey, Peter Banzer, Matthias Karg, and Nicolas Vogel*

Collective excitation of periodic arrays of metallic nanoparticles by coupling localized surface plasmon resonances to grazing diffraction orders leads to surface lattice resonances with narrow line width. These resonances may find numerous applications in optical sensing and information processing. Here, a new degree of freedom of surface lattice resonances is experimentally investigated by demonstrating handedness-dependent excitation of surface lattice resonances in arrays of chiral plasmonic crescents. The self-assembly of particles used as mask and modified colloidal lithography is applied to produce arrays of planar and 3D gold crescents over large areas. The excitation of surface lattice resonances as a function of the interparticle distance and the degree of order within the arrays is investigated. The chirality of the individual 3D crescents leads to the formation of chiral lattice modes, that is, surface lattice resonances that exhibit optical activity.

A strategy to produce metasurfaces exhibiting strong optical properties is to arrange metal nanostructures in defined lattices. The localized surface plasmon resonances (LSPRs) of the individual metal nanoparticles can be coupled to the diffractive lattice mode of the array, leading to the formation of surface lattice resonances (SLRs).^[1–4] These resonances are also called surface lattice modes or collective localized surface plasmons, but should not be confused with collective modes in plasmonic molecules that arise from near-field coupling of the parental

resonances.^[5,6] A collective excitation (SLR) possesses a reduced linewidth as compared to the excitation of the LSPRs in nanoparticle ensembles.^[1–4] Thus, SLRs can provide high quality-factor metasurfaces with substantial impact in nanophotonic and sensing applications.^[1–4]

Oblique incidence on planar metasurfaces constructed of an array of split-ring resonators showed that SLRs can also selectively respond to the handedness of circularly polarized light, causing sharp lattice-mode assisted extrinsic circular dichroism.^[7,8] The spectral position of these SLRs can be tuned by the angle of incidence, leading to the emergence of extrinsic chiral surface lattice resonances.^[9–12]

Strong optical activity can also result from plasmonic 3D nanostructures without mirror symmetry. However, SLRs from arrays of 3D building-blocks with intrinsic chirality remain unexplored, but promise decreased losses and enhanced optical activity.^[1,13]

The fabrication of chiral 3D nanostructures is challenging for both, bottom-up and top-down methods.^[14–16] Recently, the excitation of SLRs was seen in self-assembled, large area colloidal systems.^[17,18] Such systems offer the possibility for fast manufacturing and covering large-areas on different substrate materials.^[19] Colloid-based materials allow for embedding of nanoparticle arrays into flexible free-standing polymer films,^[20] enabling the design of mechanically tunable^[21] and stimuli-responsive hydrogel membranes.^[22]


Here, we use colloidal lithography^[23–25] to fabricate arrays of 3D crescents with a selective response to the handedness of incident circularly polarized light, and we experimentally demonstrate handedness-dependent (chiral) SLRs at normal incidence. Colloidal lithography^[23–25] is an experimentally simple and fast process to fabricate 3D chiral plasmonic nanostructures.^[26–28] However, a necessary condition to observe SLRs in such nanostructure arrays is that their lattice constant must be in the range of the wavelength of the LSPRs of the individual nanostructures.^[1–4] For objects with resonances in the near-infrared, such as, for example, split ring resonators, this requires large interparticle distances approaching the micrometer range. For conventional colloidal lithography processes, which depend on the controlled shrinkage of a polymer particle matrix, such distances are not easily achievable.^[12,28–30] Therefore, we use core-shell particles with rigid cores (silica) and soft, deformable polymer shells.^[31,32] The particles self-assemble into hexagonally ordered monolayers at the air/water

E. S. A. Goerlitzer, Dr. R. Mohammadi, Dr. M. Rey, Prof. N. Vogel
Institute of Particle Technology
Friedrich-Alexander University Erlangen-Nürnberg
Cauerstraße 4, Erlangen D-91058, Germany
E-mail: nicolas.vogel@fau.de

Dr. S. Nechayev, Dr. P. Banzer
Max Planck Institute for the Science of Light
Staudtstr. 2, Erlangen D-91058, Germany

Dr. S. Nechayev, Dr. P. Banzer
Institute of Optics
Information and Photonics
Friedrich-Alexander University Erlangen-Nürnberg
Staudtstr. 7/B2, Erlangen D-91058, Germany

K. Volk, Prof. M. Karg
Institut für Physikalische Chemie I: Kolloide und Nanooptik
Heinrich-Heine-Universität Düsseldorf
Universitätsstr. 1, Düsseldorf D-40225, Germany

 The ORCID identification number(s) for the author(s) of this article can be found under <https://doi.org/10.1002/adma.202001330>.

© 2020 The Authors. Published by WILEY-VCH Verlag GmbH & Co. KGaA, Weinheim. This is an open access article under the terms of the Creative Commons Attribution License, which permits use, distribution and reproduction in any medium, provided the original work is properly cited.

DOI: 10.1002/adma.202001330

interface, where the polymer shell provides a flexible spacer to separate the inorganic core particles.^[33] Our method opens the possibility of tuning the lattice constant independent of the core particle diameter. We can therefore produce nanostructure arrays with large interparticle distances required to observe SLRs. We experimentally confirm the feasibility of our methods by fabricating arrays of 3D crescents with controlled interparticle distances resulting in the appearance of chiral SLRs.

We use core-shell particles consisting of SiO₂ cores ($d = 198$ nm) with soft poly(*N*-isopropylacrylamide) (PNiPAm) shells (Figure 1a) and self-assemble them at the air/water interface of a Langmuir trough.^[33] The soft PNiPAm shell separates the silica cores, which form a non-close-packed hexagonal lattice. The interparticle distance of the silica particles in the resulting lattice can be controlled via the shell thickness or the degree of compression at the interface (Figure 1b).^[33,34] After transferring the colloidal monolayer to a substrate via the Langmuir–Blodgett technique, we remove the organic PNiPAm shell with oxygen plasma (Figure 1c). Subsequently, we employ the particle monolayer as a mask to produce arrays of chiral crescents, which exhibit structural chirality (Figure 1; details in Figure S1, Supporting Information).^[28,35,36] Initially, a layer of silicon dioxide (20 nm) is deposited by reactive silicon monoxide evaporation on a tilted substrate coated with the colloidal monolayer (elevation angle $\alpha = 30^\circ$) to deposit material underneath the particles. In the next step, the substrate is rotated by 90° , and a layer of titanium (1 nm) as an adhesion promoter and gold (40 nm) are evaporated under the same elevation angle (Figure 1e). The rotation leads to a different azimuthal angle ($\gamma = 90^\circ$) between the gold and the silicon dioxide films. Directed physical etching using Ar ions normal to the surface finally removes all material not shielded by the particle mask. The crescent-shaped nanostructures form in the substrate areas shadowed by the particles and remain on the substrate after removal of the particles (Figure 1f). The mutual rotation between the gold and the silica layer provides a dielectric step in the middle of the crescent. This step breaks the mirror symmetry and therefore induces chirality. The resulting chiroptical properties can be controlled by the thickness and the position of the dielectric step (Figure 1g,h).^[28] Side-view scanning electron microscopy images (SEM) show the 3D geometry of the produced crescents (Figure 1i,j). Achiral (flat) crescents were fabricated by the same method by omitting the silicon dioxide deposition step.^[37–39]

To support SLRs, a sample must fulfill at least four criteria: i) the plasmonic particles are arranged in a proper lattice,^[40,41] ii) with a sufficiently large domain size (≈ 20 particles),^[17,42,43] iii) with a lateral interparticle spacing that leads to grazing orders of diffraction that spectrally overlap with the LSPR,^[44] iv) within a homogenous refractive index environment.^[1,2] These criteria can be fulfilled on smaller array sizes using conventional lithography approaches, allowing for the appearance of very sharp SLR features. However, a colloid based method—covering cm² areas—inherently features small fluctuations and irregularities with respect to the lattice position. Hence, we thoroughly analyzed our produced nanostructure arrays to investigate the influence of structural imperfections on the collective plasmonic properties. We first focus on achiral planar crescents to separate the influence of structure and order of the arrays from the effects of chirality observed in the 3D crescents arrays.

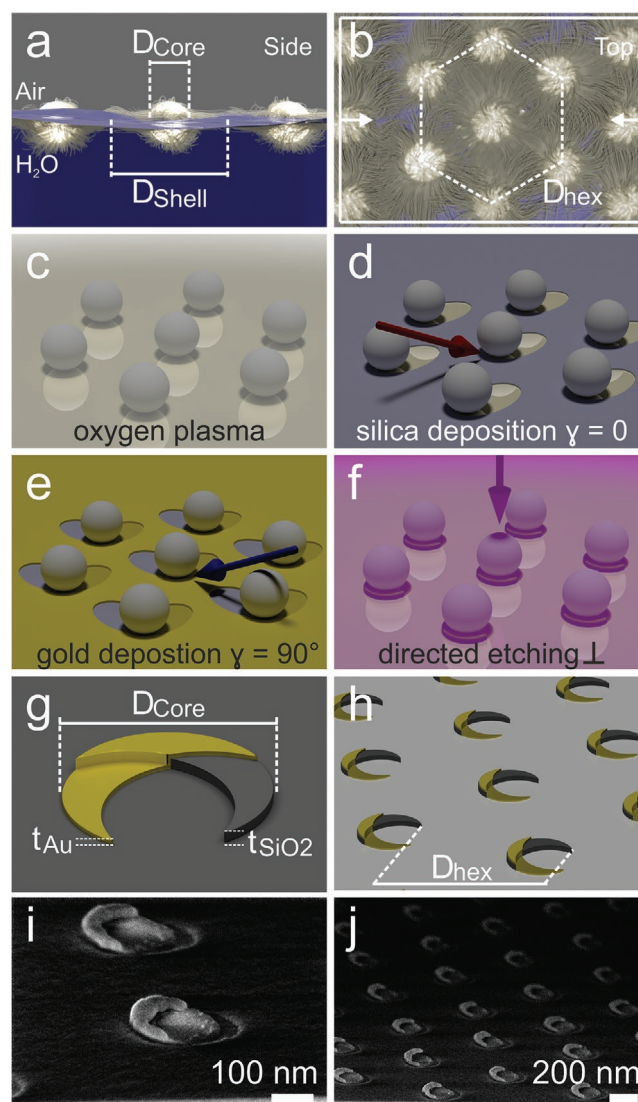


Figure 1. Schematic illustration of the colloidal lithography approach to produce arrays of chiral single crescents exhibiting chiral surface lattice resonances (SLRs). a) Structure of SiO₂–PNiPAm core-shell particles at the air/water interface showing the separation of the silica cores through the soft polymer shells. b) The nearest neighbor distance (D_{hex}) of the array can be controlled by either the shell thickness (D_{shell}) or by the degree of compression on a Langmuir trough. c) Transfer of the particle arrangement onto a glass substrate and removal of the polymer shell by oxygen plasma. d) Evaporation of silicon dioxide (20 nm) with an elevation angle of $\alpha = 30^\circ$ with respect to the surface normal. e) Evaporation of titanium (1 nm, adhesion promoter) and gold (40 nm) under an azimuthal twist angle ($\gamma = 90^\circ$) after rotation of the substrate. The enantiomeric counterpart can be produced by twisting into the opposite direction ($\gamma = -90^\circ$). f) Directed physical etching along the surface normal and removal of the particle mask using adhesive tape produces an array of crescent nanostructures. g) Illustration of the geometry of a 3D chiral crescent. h) Illustration of the final lattice composed of chiral crescents used to excite chiral SLRs. i, j) Side-view SEM images of the fabricated crescents showing details of the geometry and the arrangement in a hexagonal array.

In a previous theoretical work on lattice modes in silicon disk arrays, it was shown that lateral displacements, as well as size deviations, do not hinder the excitation of lattice modes, but significantly broaden their spectral appearance.^[45] Similar

results were also shown for colloid-based systems, where the polydispersity of gold nanoparticles influenced the Q-factor ($\lambda_{\text{SLR}}/\text{FWHM}$) of the SLRs.^[21] The diameter of our templating silica particles is $198 \text{ nm} \pm 3 \text{ nm}$, leading to a polydispersity of about 1.5% of the produced plasmonic crescents.^[33] SEM reveals the hexagonal arrangement of the prepared crescent array (Figure 2a,b), while the optical photograph of a sample with the polymeric shell on top visualizes the polycrystallinity of the sample by its structural color (Figure 2c). The grain size exceeds several square millimeters in some cases, as illustrated by the appearance of Bragg peaks under illumination of a colloidal monolayer with a hand-held 405 nm laser (Figure 2e).

To investigate lateral fluctuations inside individual grains, we took at least ten images per sample (image area $\approx 980 \mu\text{m}^2$) of four crescent arrays with varying lattice constants. All images were recorded before removing the masking silica particles. We identified individual particles in each image and calculated their corresponding radial distribution functions ($g^2(r)$, pair correlation functions). We averaged the radial distribution functions of the individual images, and normalized their radii to the nearest-neighbor distance D_{hex} . The radial distribution functions of all samples indicate at least four periods of ordering. Thus, we expect that the single crystalline domains contain at least 31 particles, which is sufficient to support SLRs.^[17,42,43] Figure 2d exemplarily shows the analysis of two characteristic samples with different interparticle distances ($D_{\text{hex}} = 658 \text{ nm}$ and 684 nm ; see Figure S2a, Supporting Information, for the full set of samples). As a result of the normalization, the peak at $r/D_{\text{hex}} = 1$ appears as the global maximum (Figure 2d). The small peak at shorter distances ($r/D_{\text{hex}} < 1$) is

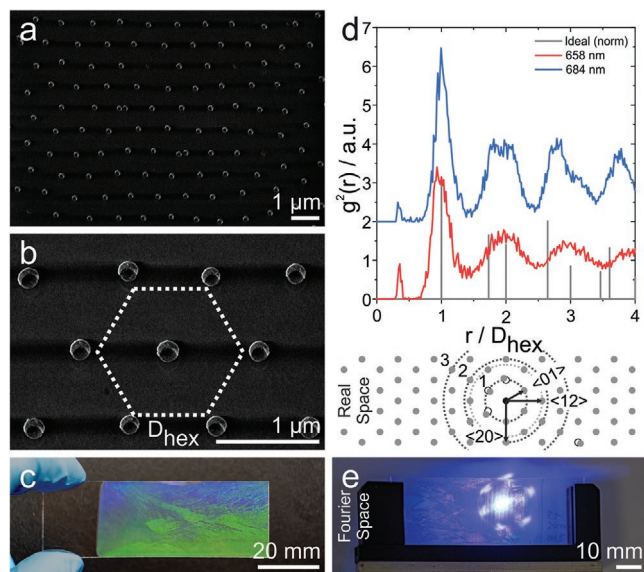


Figure 2. Structural analysis of arrays of planar, achiral crescents. a,b) Low- and high-magnification SEM images of a crescent array with $D_{\text{hex}} = 870 \text{ nm}$. The images highlight the typical ordering of such large-area samples prepared by the self-assembly process. c) Optical photograph of the self-assembled core-shell particles on a glass substrate. d) Averaged radial distribution function ($g^2(r)$, pair correlation function) with the radii normalized to the nearest-neighbor distance (r/D_{hex}) for two exemplary samples (658 and 684 nm). e) Bragg reflections visible on a screen behind the sample upon illumination with a 405 nm laser pointer, indicating a macroscopic order within the sample.

caused by particle duplet impurities. However, it appears with a very small probability. The sharper and more distinct peaks in the radial distribution function clearly show the higher degree of order of the sample with $D_{\text{hex}} = 684 \text{ nm}$ compared to the sample with $D_{\text{hex}} = 658 \text{ nm}$ (details in Figure S2, Supporting Information).

Figure 3 compares the simulated and experimental optical properties of planar crescent arrays. We measured transmission spectra of linearly polarized light using a commercial UV-vis-IR spectrometer (Figure 3a). We match the refractive index (RI) by an oil ($n = 1.518$) sandwiched between the substrate and a glass cover slip. The collimation angle in this instrument is approximately 3° , which will further broaden the measured spectra (details in Supporting Information).

If measured in air, the planar crescent array with $D_{\text{hex}} = 684 \text{ nm}$ shows an LSPR at around 830 nm (Figure 3b, dashed lines) when illuminated with polarization in the Y direction, that is, parallel to the short axis of the crescents, typically termed U1 resonance. For light polarized along the X direction, that is, parallel to the long axis of the crescents, a dipolar resonance is excited at 1250 nm, and a quadrupolar resonance appears at 677 nm. These resonances have historically been termed C1 and C2, respectively, as the crescent reads as a letter “C” for a polarization along the long axis, and as a letter “U” for the short axis.^[37,38] For a more convenient comparison with literature, we use both nomenclatures (X/C and Y/U) simultaneously.

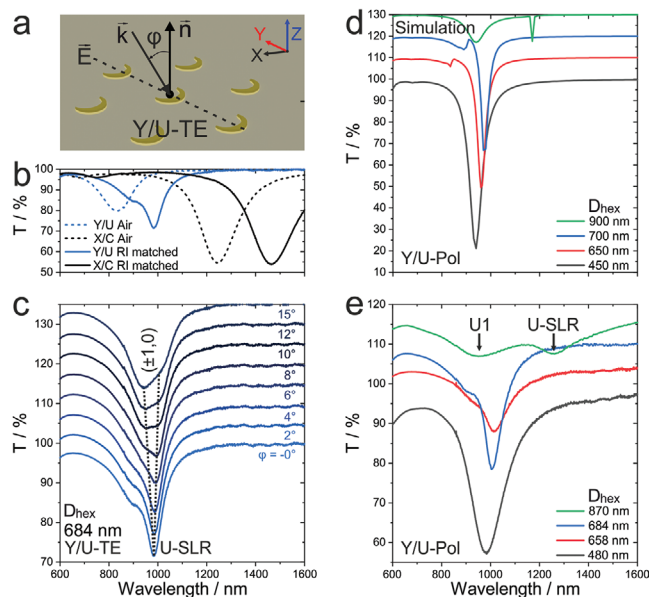


Figure 3. Simulated and measured optical response of planar achiral crescent arrays to linearly Y/U-TE polarized light. a) Schematic illustration of the excitation scheme and relative orientations of the nanostructure and the incident light beam for the incident Y/U-TE polarization used in experiments and simulations. b) Spectra of the sample with $D_{\text{hex}} = 684 \text{ nm}$ with and without refractive index matching. With homogeneous refractive index, a surface lattice resonance (U-SLR) appears for the incident Y/U-TE polarization c) Angle-resolved optical measurements, obtained by tilting the sample, show a splitting of the U-SLR in the diffraction orders (1,0)/(-1,0) for the same sample. Spectra are shifted upward by 5% for clarity. d) Simulated spectra of hexagonal crescent arrays with D_{hex} between 450 and 900 nm for the incident Y/U polarization. Spectra are shifted upward by 10%. e) Experimentally measured spectra of crescent arrays with similar lattice constants as in (d). Spectra are shifted upward by 5%.

The optical response drastically changes upon RI matching with the substrate (Figure 3b, solid lines). Due to the increased refractive index, the C/X resonances (C1, C2) are slightly broadened and red-shifted to 1465 nm and 748 nm, respectively. The U1 resonance is now able to couple to a Bragg mode,^[1–3] as seen by the splitting of the resonance into two peaks. Beside the LSPR, which is diminished in strength, an SLR in U polarization (U-SLR) appears at 984 nm. Once the sample is tilted and illuminated with Y/U-TE polarized light (Figure 3a), we see the presence of diffraction orders (1,0) and (–1,0) (Figure 3c) with a vanishing band-edge mode (U-SLR). A similar behavior has recently been demonstrated for the C2 resonance of crescent-shaped nanostructures arranged in a square lattice and further indicates the diffractive nature of the resonance.^[41,46]

Next, we investigate the dependence of the U-SLRs on the interparticle distance (D_{hex}) of the nanostructure arrays (Figure 3d,e). If the interparticle distances of the arrays are too small, the resonances broaden compared to individual spectra.^[47] At $D_{\text{hex}} > 600$ nm, the grazing diffraction orders start to couple to the localized U1 resonance and U-SLRs are observed due to sufficient spectral overlap of the two resonances. With increasing lattice constants, the (1,0) Bragg mode shifts to longer wavelengths, that is, further away from the LSPR. Thus, the coupling efficiency decreases until the U-SLR vanishes for D_{hex} significantly above 900 nm (see full set of the simulated spectra in Figure S3c, Supporting Information). The near fields for the U1 resonance visible in the electromagnetic field maps (Figure S4, Supporting Information) confirm the hybrid character of the SLR, resulting from diffractive/plasmonic coupling. The experimental spectra with similar lattice constants match the simulated results (Figure 3e). The SLR evolves for interparticle distances larger than 600 nm and shifts to longer wavelengths with increasing interparticle distances. The different degrees of order of the two samples with $D_{\text{hex}} = 658$ nm and $D_{\text{hex}} = 684$ nm seen in the radial distribution functions (Figure 2) are reflected in the experimental transmission spectra. The latter sample shows sharper and more defined resonances. Similarly, the broadening of the resonances in the sample with the largest interparticle distance ($D_{\text{hex}} = 870$ nm) compared to the simulated spectra is caused by lattice imperfections in the experimental system. We also observe a systematic red-shift of the resonances in the experimental spectra compared to the simulations, which may be caused by surface roughness or minor deviations in the exact crescent dimensions and has been observed in similar systems.^[39]

Next, we numerically investigate the response of arrays of 3D chiral crescents (Figure 4). For small lattice constants (e.g., $D_{\text{hex}} = 400$ nm), we observe the excitation of the three LSPRs with circularly polarized light, without SLRs (Figure 4a). The difference between right- and left-hand circularly polarized (RCP, LCP) light ($\Delta T = T_{\text{RCP}} - T_{\text{LCP}}$) is shown in Figure 4b. The U1 and C1 resonances show different signs in the differential transmission, in agreement with the behavior of individual chiral crescents.^[28] This means that this enantiomer of the chiral crescents (azimuthal twisting angle $\gamma = +90^\circ$) transmits more LCP light at the U1 resonance, and more RCP at the C1 resonance (solid and dashed lines respectively in Figure 4a). We previously explained the sign and origin of the differential transmission of LCP and RCP of individual crescents using a point-dipole approximation to analyze the magneto-electric

polarizability.^[28,48,49] In this model, the chiral response results from simultaneous excitation of electric and magnetic dipole moments that couple with different efficiency to incident LCP and RCP polarized electromagnetic waves.^[50,51]

With increasing lattice constant, an SLR emerges (Figure 4a), which confirms that the LSPRs of chiral crescents also couple to grazing diffraction orders of the lattice, similar to the planar achiral crescents discussed above. The (1,0) diffraction mode of the lattice couples to the U1 resonance (U-SLR, along the $\langle 12 \rangle$ direction of the lattice) for smaller lattice constants. At larger lattice constants, where the diffraction wavelength spectrally overlaps with the C1 resonance, SLRs arise from diffractive coupling to the C1 resonance (C-SLR, along the $\langle 01 \rangle$ direction of the lattice). The different nature of the LSPRs (U1, C1) and the SLRs (U-SLR, C-SLR) can also be illustrated by their near fields (Figure 4c,d). The SLRs in arrays of chiral crescents clearly show their periodic nature and a continuous twisting of the electric fields, which differs from the uniform field direction observed for the achiral lattice mode in the planar crescent array (details in Figure S5, Supporting Information). The current distributions within the individual nanostructures (Figure 4d) show the typical near-field characteristics of the U and C resonances.^[28]

Interestingly, the SLRs show a selective response to circularly polarized light, where the sign of the differential transmission follows the trend observed for the LSPRs in the uncoupled state; that is, U-SLRs show a negative and the C-SLRs a positive ΔT for this enantiomer of the structures (Figure 4b). In other words, the proposed nanostructure platform supports the excitation of chiral SLRs. Furthermore, the magnitude of the differential transmission of these SLRs exceeds that of the LSPR peak transmission for both the U-SLR (e.g. ≈ 3.7 -fold increase for $D_{\text{hex}} = 600$ nm), and the C-SLR (e.g. ≈ 6.6 -fold increase for $D_{\text{hex}} = 950$ nm) and undergo a spectral narrowing (calculated quality factors can be found in Figure S6, Supporting Information).

In a proof-of-principle experiment, we demonstrate the excitation of chiral SLRs for two lattices of chiral crescents with $D_{\text{hex}} \approx 684$ nm and $D_{\text{hex}} \approx 870$ nm, which have shown effective coupling of the Bragg mode to the U1 resonance (Figures 2 and 3). We first measure the transmission of linearly polarized light at normal incidence to identify the different resonances (Figure 5a,b). These spectra of the chiral crescents resemble the spectra of their achiral analogues (Figure 3e) and enable us to identify the SLRs (U-SLR) for the incident Y/U polarization (highlighted by arrows in all spectra).

Next, we repeat the experiment with RCP and LCP light. The resulting transmission spectra (Figure 5c) show the same dominant resonances as for the incident linearly polarized light (Figure 5b), including the U-SLR for both interparticle distances ($D_{\text{hex}} \approx 684, 870$ nm). The differential transmission spectra show clear peaks at the spectral positions of the SLRs highlighted by the vertical arrows in Figure 5d. The peaks in both samples show the same sign of ΔT as the localized U1 resonance. The appearance of these peaks demonstrates the presence of chiral band-edge lattice modes in our system. In contrast to planar objects, which can only exhibit chiral lattice-modes under oblique illumination,^[7] the chiroptical response in our SLRs is caused by the intrinsic chirality of the 3D building blocks.

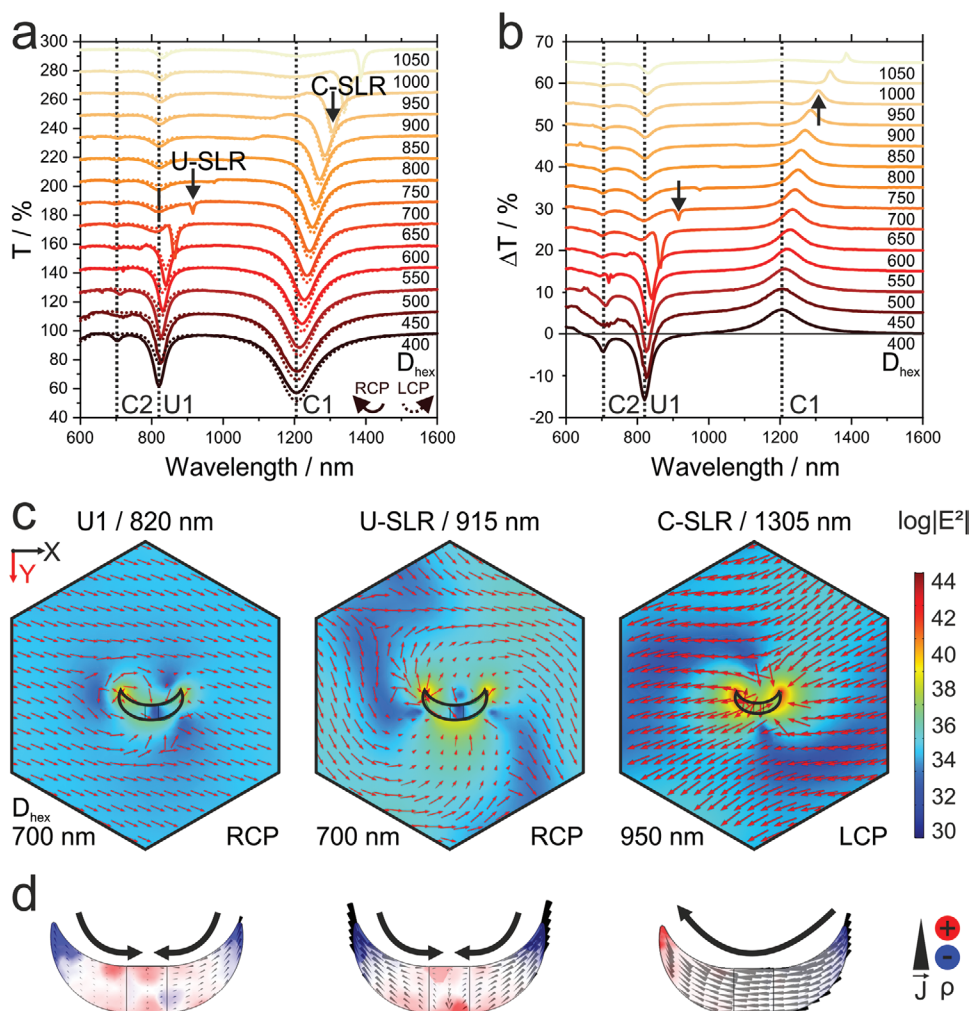


Figure 4. Simulated optical response of arrays of 3D chiral crescents to circularly polarized light. a) Spectra for right and left circularly polarized light of arrays with D_{hex} between 400 and 1050 nm. The simulated crescents have a thickness of 40 nm, and a silicon dioxide step height of 20 nm. With increasing interparticle distance D_{hex} , the SLR first couples to the U1 resonance (U-SLR) and then to the C1 resonance (C-SLR). Spectra are shifted upward by 15%. b) Differential transmission (ΔT) spectra for the same arrays, showing the selective response of the SLR to circularly polarized light with different signs of ΔT : The U-SLR shows a negative sign, while the C-SLR shows a positive sign. Spectra are shifted upward by 5%. c) Normalized logarithmic electric field maps and d) current distributions of the LSPR (U1), its U-SLR (for $D_{\text{hex}} = 700$ nm), and the C-SLR for larger interparticle distances ($D_{\text{hex}} = 950$ nm).

In conclusion, we applied a modified self-assembly technique with soft core-shell particles to fabricate arrays of plasmonic crescent nanostructures with large lattice constants. The large lattice constants feature spectrally overlapping in-plane diffraction modes and localized surface plasmon resonances. Therefore, they allow for the observation of surface lattice resonances. We first investigated the excitation of SLRs in achiral crescents as a function of the lattice constant of the array and correlate their spectral properties with the degree of order in the sample. Using chiral crescents as the building blocks in the array does not alter the diffractive properties of the system. The chiral nature of the building blocks, however, leads to the excitation of intrinsically chiral SLRs that selectively respond to the handedness of incident circularly polarized light. The presented chiral 3D-metasurfaces may find applications in enhanced chiral sensing, handedness-selective coupling to guided modes, control of circularly polarized fluorescence emission, or the design of polarization-selective mirrors.

Experimental Section

Synthesis of SiO_2 @PNIPAM Core-Shell Particles: The synthesis is described in more detail in ref. [33]. Purchased chemicals and more details can be found in Supporting Information. Silica nanoparticles with a diameter of 198 nm were synthesized via the standard Stöber method.^[52] 102.7 μL MPS (3.9×10^{-4} mmol) were subsequently added and the dispersion stirred for 1 day at 50°C and 60 min at 100°C. The PNIPAM shell was formed by precipitation polymerization using 282.9 mg NIPAM (2.5 mmol, 50 mmol L^{-1}) and the respective amount of BIS (Table S1, Supporting Information) in a nitrogen atmosphere.^[33] The particles were purified by centrifugation prior to use.

Self-Assembly and Colloidal Lithography: The assembly is described in detail in ref. [33]. In brief, the SiO_2 @PNIPAM core-shell particles were assembled at the air/water interface of a Langmuir-Blodgett trough and transferred to a cleaned microscope slide (EtOH, oxygen plasma) at different surface pressures to achieve the different lattice constants (details in Table S1, Supporting Information).^[33] The polymeric shells were removed by oxygen plasma treatment (4 sccm O_2 , 100 W, 8 min; Femto SLS, Diener, Germany). Planar crescents were fabricated by angular metal deposition and directed etching steps following protocols

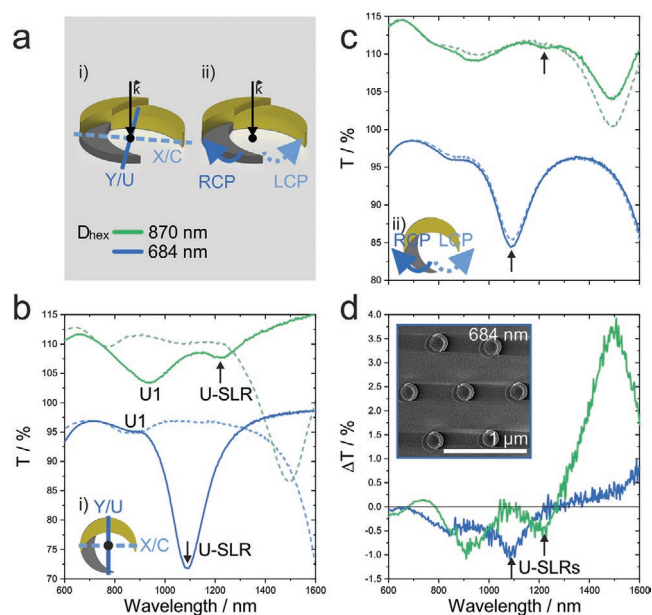


Figure 5. Chiroptical properties of arrays of 3D chiral crescents with interparticle distances of $D_{\text{hex}} \approx 684$ nm (blue lines) and $D_{\text{hex}} \approx 870$ nm (green lines). a) Schematic illustration of the experimental conditions and orientations. b) Illumination with linearly polarized light along the Y/U axis (solid lines) shows the localized U1 resonances and their associated lattice modes (U-SLR; highlighted by arrows). c) Illumination with circularly polarized light excites the same resonances attainable using incident linearly polarized light, but with different absolute values of transmission for RCP (solid lines) and LCP (dashed lines). d) The differential transmission shows peaks at the spectral positions of the LSPRs. An additional peak in both samples at the spectral position of the SLRs arises (indicated by arrows), demonstrating their chiral nature.

from literature (details in Supporting Information).^[37–39] The fabrication of the 3D chiral crescents is based on a modified on-edge colloidal lithography approach using a series of angular deposition steps described in the literature.^[28] The difference to the planar crescents was the presence of a silicon dioxide step in the middle of the crescents (details in Supporting Information). Gold was chosen as the material for the nanostructures because of its inertness and silicon dioxide as the spacer layer to match the glass substrate.

Characterization: SEM images were taken using a GeminiSEM 500 (Zeiss, Germany). UV–vis–NIR spectra were measured using a conventional spectrometer (Lambda 950, Perkin-Elmer) with a Glan Thompson polarizer drive (Perkin-Elmer, B050-5284). Circularly polarized light was obtained by inserting an additional quarter wave-plate (B.Halle, 600–2700 nm, super achromatic) with the fast axis rotated by $\pm 45^\circ$ with respect to the linear polarization to obtain left or right circularly polarized light.

FEM Simulation: COMSOL Multiphysics was used with a hexagonal unit cell, periodic boundary conditions, and perfectly matched layer (PML) in Z-direction to simulate spectra between 600 and 1600 nm in 5 nm steps. The optical constants of gold were taken from experimental data.^[53] The refractive index of the environment was 1.5. The illuminations were two orthogonally polarized monochromatic plane waves. To obtain circularly polarized light, linear combinations of the aforementioned orthogonal illuminations with $-\pi/2$ phase difference were applied.

Supporting Information

Supporting Information is available from the Wiley Online Library or from the author.

Acknowledgements

This project received funding from the European Union's Horizon 2020 research and innovation programme under grant agreement No 861950, project POSEIDON. N.V. acknowledges support from the Interdisciplinary Center for Functional Particle System (FPS) at FAU Erlangen-Nürnberg. M.K. acknowledges the German Research Foundation (DFG) for funding through the Emmy Noether programme under grant KA3880/1-1.

Conflict of Interest

The authors declare no conflict of interest.

Keywords

chirality, colloidal lithography, optical activity, plasmonics, surface lattice resonances

Received: February 25, 2020

Revised: March 23, 2020

Published online: April 21, 2020

- [1] V. G. Kravets, A. V. Kabashin, W. L. Barnes, A. N. Grigorenko, *Chem. Rev.* **2018**, *118*, 5912.
- [2] F. J. G. De Abajo, *Rev. Mod. Phys.* **2007**, *79*, 1267.
- [3] W. Wang, M. Ramezani, A. I. Väkeväinen, P. Törmä, J. G. Rivas, T. W. Odom, *Mater. Today* **2018**, *21*, 303.
- [4] C. Cherqui, M. R. Bourgeois, D. Wang, G. C. Schatz, *Acc. Chem. Res.* **2019**, *52*, 2548.
- [5] F. Wen, J. Ye, N. Liu, P. Van Dorpe, P. Nordlander, N. J. Halas, *Nano Lett.* **2012**, *12*, 5020.
- [6] A. Ahmadvand, N. Pala, D. Ö. Güney, *Opt. Express* **2015**, *23*, A682.
- [7] I. De Leon, M. J. Horton, S. A. Schulz, J. Upham, P. Banzer, R. W. Boyd, *Sci. Rep.* **2015**, *5*, 13034.
- [8] I. Sersic, M. A. van de Haar, F. B. Arango, A. F. Koenderink, *Phys. Rev. Lett.* **2012**, *108*, 223903.
- [9] M. Cotrufo, C. I. Osorio, A. F. Koenderink, *ACS Nano* **2016**, *10*, 3389.
- [10] S. Chen, B. Reineke, G. Li, T. Zentgraf, S. Zhang, *Nano Lett.* **2019**, *19*, 6278.
- [11] W. Liu, L. Mei, Y. Li, L. Yu, Z. Lai, T. Yu, H. Chen, *Opt. Lett.* **2019**, *44*, 5868.
- [12] L. Cao, J. Qi, Q. Wu, Z. Li, R. Wang, J. Chen, Y. Lu, W. Zhao, J. Yao, X. Yu, Q. Sun, J. Xu, *Nanoscale Res. Lett.* **2019**, *14*, 388.
- [13] M. Qiu, L. Zhang, Z. Tang, W. Jin, C.-W. Qiu, D. Y. Lei, *Adv. Funct. Mater.* **2018**, *28*, 1803147.
- [14] C. M. Soukoulis, M. Wegener, *Nat. Photonics* **2011**, *5*, 523.
- [15] Z. Liu, Y. Xu, C. Ji, S. Chen, X. Li, X. Zhang, Y. Yao, J. Li, *Adv. Mater.* **2020**, *32*, 1907077.
- [16] M. J. Urban, C. Shen, X.-T. Kong, C. Zhu, A. O. Govorov, Q. Wang, M. Hentschel, N. Liu, *Annu. Rev. Phys. Chem.* **2019**, *70*, 275.
- [17] K. Volk, J. P. S. Fitzgerald, P. Ruckdeschel, M. Retsch, T. A. F. König, M. Karg, *Adv. Opt. Mater.* **2017**, *5*, 1600971.
- [18] M. Juodėnas, T. Tamulevičius, J. Henzie, D. Erts, S. Tamulevičius, *ACS Nano* **2019**, *13*, 9038.
- [19] Y. Brasse, V. Gupta, H. C. T. Schollbach, M. Karg, T. A. F. König, A. Fery, *Adv. Mater. Interfaces* **2019**, *7*, 1901678.
- [20] K. Volk, J. P. S. Fitzgerald, M. Karg, *ACS Appl. Mater. Interfaces* **2019**, *11*, 16096.

- [21] V. Gupta, P. T. Probst, F. R. Goßler, A. M. Steiner, J. Schubert, Y. Brasse, T. A. F. König, A. Fery, *ACS Appl. Mater. Interfaces* **2019**, *11*, 28189.
- [22] N. Gisbert Quilis, M. van Dongen, P. Venugopalan, D. Kotlarek, C. Petri, A. Moreno Cencerrado, S. Stanescu, J. L. Toca Herrera, U. Jonas, M. Möller, A. Mourran, J. Dostalek, *Adv. Opt. Mater.* **2019**, *7*, 1900342.
- [23] A. Nemiroski, M. Gonidec, J. M. Fox, P. Jean-Remy, E. Turnage, G. M. Whitesides, *ACS Nano* **2014**, *8*, 11061.
- [24] B. Ai, H. Möhwald, D. Wang, G. Zhang, *Adv. Mater. Interfaces* **2017**, *4*, 1600271.
- [25] Z. Wang, B. Ai, H. Möhwald, G. Zhang, *Adv. Opt. Mater.* **2018**, *6*, 1800402.
- [26] B. Frank, X. Yin, M. Schäferling, J. Zhao, S. M. Hein, P. V. Braun, H. Giessen, *ACS Nano* **2013**, *7*, 6321.
- [27] V. E. Bochenkov, D. S. Sutherland, *Opt. Express* **2018**, *26*, 27101.
- [28] E. S. A. Goerlitzer, R. Mohammadi, S. Nechayev, P. Banzer, N. Vogel, *Adv. Opt. Mater.* **2019**, *7*, 1801770.
- [29] M. Retsch, M. Tamm, N. Bocchio, N. Horn, R. Förch, U. Jonas, M. Kreiter, *Small* **2009**, *5*, 2105.
- [30] N. Vogel, S. Goerres, K. Landfester, C. K. Weiss, *Macromol. Chem. Phys.* **2011**, *212*, 1719.
- [31] M. Karg, *Macromol. Chem. Phys.* **2016**, *217*, 242.
- [32] M. Karg, S. Wellert, S. Prevost, R. Schweins, C. Dewhurst, L. M. Liz-Marzán, T. Hellweg, *Colloid Polym. Sci.* **2011**, *289*, 699.
- [33] J. S. J. Tang, R. S. Bader, E. S. A. Goerlitzer, J. F. Wendisch, G. R. Bourret, M. Rey, N. Vogel, *ACS Omega* **2018**, *3*, 12089.
- [34] M. Rey, M. A. Fernandez-Rodriguez, M. Karg, L. Isa, N. Vogel, *Acc. Chem. Res.* **2020**, *53*, 414.
- [35] K. Dietrich, D. Lehr, C. Helgert, A. Tünnermann, E.-B. Kley, *Adv. Mater.* **2012**, *24*, OP321.
- [36] K. Dietrich, C. Menzel, D. Lehr, O. Puffky, U. Hübner, T. Pertsch, A. Tünnermann, E. B. Kley, *Appl. Phys. Lett.* **2014**, *104*, 193107.
- [37] J. S. Shumaker-Parry, H. Rochholz, M. Kreiter, *Adv. Mater.* **2005**, *17*, 2131.
- [38] H. Rochholz, N. Bocchio, M. Kreiter, *New J. Phys.* **2007**, *9*, 53.
- [39] N. Vogel, J. Fischer, R. Mohammadi, M. Retsch, H.-J. Butt, K. Landfester, C. K. Weiss, M. Kreiter, *Nano Lett.* **2011**, *11*, 446.
- [40] A. D. Humphrey, W. L. Barnes, *Phys. Rev. B Condens. Matter Mater. Phys.* **2014**, *90*, 075404.
- [41] R. Guo, T. K. Hakala, P. Törmä, *Phys. Rev. B* **2017**, *95*, 155423.
- [42] F. Xie, W. Wu, M. Ren, W. Cai, J. Xu, *Adv. Opt. Mater.* **2020**, *8*, 1901435.
- [43] S. R. K. Rodriguez, M. C. Schaafsma, A. Berrier, J. Gmez Rivas, *Phys. B Condens. Matter* **2012**, *407*, 4081.
- [44] A. A. Maradudin, I. Simonsen, J. Polanco, R. M. Fitzgerald, *J. Opt.* **2016**, *18*, 024004.
- [45] V. I. Zakomirnyi, S. V. Karpov, H. Ågren, I. L. Rasskazov, *J. Opt. Soc. Am. B* **2019**, *36*, E21.
- [46] Y. Lin, D. Wang, J. Hu, J. Liu, W. Wang, J. Guan, R. D. Schaller, T. W. Odom, *Adv. Funct. Mater.* **2019**, *29*, 1904157.
- [47] I. Sersic, M. Frimmer, E. Verhagen, A. F. Koenderink, *Phys. Rev. Lett.* **2009**, *103*, 213902.
- [48] D. G. Baranov, B. Munkhbat, N. O. Länk, R. Verre, M. Käll, T. Shegai, *Nanophotonics* **2020**, *9*, 283.
- [49] P. Woźniak, I. De Leon, K. Höflich, C. Haverkamp, S. Christiansen, G. Leuchs, P. Banzer, *Opt. Express* **2018**, *26*, 1513.
- [50] Z. Fan, A. O. Govorov, *Nano Lett.* **2010**, *10*, 2580.
- [51] A. O. Govorov, Z. Fan, P. Hernandez, J. M. Slocik, R. R. Naik, *Nano Lett.* **2010**, *10*, 1374.
- [52] W. Stöber, A. Fink, E. Bohn, *J. Colloid Interface Sci.* **1968**, *26*, 62.
- [53] R. L. Olmon, B. Slovick, T. W. Johnson, D. Shelton, S. H. Oh, G. D. Boreman, M. B. Raschke, *Phys. Rev. B – Condens. Matter Mater. Phys.* **2012**, *86*, 235147.